HYDROGEN, FUEL CELL & ENERGY STORAGE
ECSI IHFCA IROST

Numerical Analysis of the Effect of Pin Dimensions on the Performance of a Polymer Electrolyte Membrane Fuel Cell Featuring a Honeycomb Pin Flow Field

Ebrahim Afshari[a,*] | **Nabi Jahantigh**[b]

[a] Department of Mechanical Engineering, Faculty of Engineering, University of Isfahan, Isfahan, Iran
[b] Department of Mechanical Engineering, Faculty of Engineering, University of Zabol, Zabol, Iran
[*] Corresponding author, Email: e.afshari@eng.ui.ac.ir

Article Information

Article Type
RESEARCH ARTICLE

Article History
RECEIVED: *13 Mar 2025*
REVISED: *10 Oct 2025*
ACCEPTED: *10 Dec 2025*
PUBLISHED ONLINE: *05 Jan 2026*

Keywords

Polymer electrolyte membrane fuel cell
Honeycomb flow field
Pin
Geometric parameters
Computational fluid dynamics

Abstract

The performance of polymer electrolyte membrane (PEM) fuel cells is heavily influenced by the design of the gas flow field, especially on the cathode side. An effective flow field configuration ensures optimal reactant gas distribution, uniform current density, efficient water and heat management, and improved overall fuel cell efficiency. A novel honeycomb flow field design featuring hexagonal pins, as opposed to traditional channel-based designs, demonstrates potential for enhancing fuel cell performance. The dimensions of the pins and the channels housing them are crucial design factors in this novel approach. This study presents a three-dimensional model that numerically solves the equations of continuity, momentum, energy, charge conservation, and electrochemical kinetics across different regions of the fuel cell using a single-domain methodology. The investigation focuses on how variations in the dimensions of the channels and pins within the honeycomb flow field influence the overall performance of the fuel cell. Key design objectives include achieving uniform distribution of reactant gases and current density, enhancing voltage and power density, and minimizing pressure drop. The findings reveal that in a fuel cell equipped with a honeycomb flow field, the velocity within the pin region is significantly higher, leading to improved oxygen transport to the catalyst layer. The strategic arrangement and dimensions of the pins contribute to a more uniform distribution of oxygen and power density. While this innovative flow field design increases cell voltage and power density, it also results in a higher pressure drop compared to conventional parallel-channel configurations.

Cite this article: Afshari, E., Jahantigh, N. (2026). Numerical Analysis of the Effect of Pin Dimensions on the Performance of a Polymer Electrolyte Membrane Fuel Cell Featuring a Honeycomb Pin Flow Field. DOI: 10.22104/hfe.2025.7177.1327

Publisher: Iranian Research Organization for Science and Technology (IROST)
DOI: 10.22104/hfe.2025.7177.1327

1 Introduction

Polymer electrolyte membrane (PEM) fuel cells are versatile, capable of delivering power outputs ranging from a few watts to several megawatts. With an electrical efficiency of approximately 45% – the highest among all fuel cell types – they are highly efficient. Operating at low temperatures, these fuel cells also feature rapid startup capabilities and high power density, making them an ideal choice for transportation applications. While the flow field design has minimal impact on fuel cell performance at higher operating voltages, its importance grows at lower voltages, where concentration and mass transfer losses become significant. Under these conditions, the design and configuration of the flow field are critical to the cell's performance. The arrangement and shape of the flow field are essential for achieving uniform reactant gas distribution and efficiently managing and removing water produced within the flow channels. Numerous designs have been proposed for the flow field in polymer electrolyte membrane fuel cells. Developing an effective flow field design is a complex challenge, requiring careful consideration of multiple interdependent constraints that often have conflicting impacts on fuel cell performance. For example, serpentine flow fields ensure relatively uniform reactant distribution across the catalyst layers, leading to high current density and enhanced cell performance. However, this configuration also results in substantial pressure losses due to the extended flow path. Conversely, spiral flow fields maintain adequate electrochemical performance but experience a significant overall pressure drop due to the extended channel length and minor losses at bends [1–3].

Other designs, such as parallel, pin, and serpentine flow fields, each offer unique advantages and disadvantages. Parallel flow fields exhibit a low pressure drop; however, they often suffer from non-uniform reactant distribution across the active electrode-membrane assembly, resulting in reduced electrochemical reaction efficiency and overall fuel cell performance. Pin-type flow fields, also known as networked flow fields, consist of protrusions arranged in a grid-like pattern across the bipolar plate. This design is among the most widely used, offering multiple flow routes and minimal pressure loss. Additionally, pin-type flow fields enhance the contact area between reactant gases and the gas diffusion layer. Commonly, cubic and cylindrical pins are employed, with both anode and cathode bipolar plates featuring a matrix of machined pins to facilitate the flow of reactant gases. Essentially, the gases navigate through a network of interconnected parallel and series pathways. The gas flow tends to favor paths with lower resistance, which can lead to stagnant regions where the gas supply is insufficient. In these stagnant areas, reaction kinetics are typically slower, resulting in uneven current generation, inefficient water removal, and a reduction in fuel cell performance. Moreover, recirculation zones may form behind each pin, causing uneven distribution of reactant gases across the gas diffusion layer and affecting the catalyst surface. The flow in these small channels is slow, leading to low Reynolds numbers. This phenomenon leads to reduced reactant gas concentrations in these regions and decreased fuel cell performance. These issues are partially addressed in honeycomb flow fields.

Honeycomb flow fields feature hexagonal pins that provide more efficient pathways for fuel or oxidant distribution in all directions within a flow field between the inlet and outlet manifolds, improving both fluid and product distribution. Honeycomb flow fields in fuel cells fulfill the following requirements [4]. (a) Low pressure drop within the cell (b) Minimal stagnant regions in the flow field (c) Enhanced product removal (d) Enhanced fuel cell efficiency in comparison to traditional pin-type flow fields. The dimensions of the channels and pins in a honeycomb flow field significantly impact fuel cell performance and should be carefully considered. Computational fluid dynamics (CFD) can be used to model various phenomena in cells with different geometries and to assess the impact of channel and pin dimensions on fuel cell performance. Examples of pin-type flow field arrangements were used by Rieger and Sawyer [5], where the flow distribution network consists of numerous pins arranged in a systematic pattern. Hsieh et al. [6] carried out experiments to examine the impact of various operating parameters on the performance of a polymer electrolyte membrane (PEM) micro fuel cell using three distinct flow field configurations: serpentine, pin, and spiral. The study concluded that a specific geometry could be selected from the three flow patterns depending on the desired performance objective.

Additionally, Maia et al. [7] developed a mathematical model to simulate both the complete oxidation of ethanol and the partial oxidation producing byproducts on platinum-based catalysts in a methanol fuel cell. The flow within the channels was assumed to be laminar and steady-state, with analyses conducted under both isothermal and non-isothermal conditions. The study examined various flow field designs, including serpentine, pin, and spiral configurations. The serpentine flow field design yielded the most favorable results in isothermal simulations, while the spiral flow field performed best under non-isothermal conditions. Wang et al. [8] investigated various flow field configurations, including parallel, pin, and metal foam arrangements on the cathode side, to assess their effects on the performance of a polymer electrolyte membrane (PEM) fuel cell. The PEM fuel cell stack used was of the cathode-fed type, and polarization curves, along with electrochemical impedance spectroscopy, were recorded and analyzed for the three configurations. The results showed that the metal foam flow field configuration outperformed the others in terms of fuel cell performance.

Lobato et al. [9] investigated the current density distribution across four different flow field designs: four-pass serpentine, pin, parallel, and serpentine. Their findings revealed that both the serpentine and pin flow fields achieved a 25% increase in power density when oxygen was used as the oxidant. However, when air was used as the oxidant, the serpentine flow field exhibited the best performance among the designs. Vaz [10] applied Murray's law to introduce branching in the flow channels of a PEM fuel cell. A pin-type flow field was employed to address competing objectives such as pressure drop, manufacturability, flow velocity standard deviation, and channel area, aiming for multi-objective optimization. Similar results were obtained in the single-objective optimization, confirming the effectiveness of Murray's law in both optimization approaches.

Taghipour et al. [11] conducted a numerical evaluation of an air-cooled PEM fuel designed for UAV applications. They employed a three-dimensional, multiphase, non-isothermal model incorporating a bean-shaped pin-type flow field and compared its performance to a cell with parallel channels. The results indicated that increasing the air stoichiometry for cooling was beneficial in the bean-shaped configuration, with the maximum temperature along the channel reaching 331.5 K at a stoichiometry of 30. Yan et al. [12] studied the impact of a channel flow field containing a blocking obstacle (similar to a pin) on the performance of a polymer electrolyte membrane (PEM) fuel cell. Three distinct flow field topologies were investigated, each examined with three different surface area ratios of 0.6, 1, and 1.5. The results demonstrated that the second and third flow field designs outperformed the parallel flow field configuration, indicating that the blocking effect of the obstacle within the fuel channel improved gas transport and overall cell efficiency.

In the study conducted by Titkamol et al. [13], the performance of a fuel cell with a serpentine cathode flow field and a central obstacle was examined experimentally. The findings revealed that when oxygen was used as the oxidant, both geometries displayed similar performance levels. Conversely, when air was used as the oxidant, the maximum power output in the serpentine flow field with a blocking obstacle was approximately 1.12 to 1.3 times higher than that of the conventional flow field, depending on the air flow rate. Geo et al. [14] developed an optimal model for a PEM fuel cell with a pin-type flow configuration using a network approach. This model was constructed by establishing flow relationships within the channel network and defining an objective function, which was then solved using a quasi-Newton algorithm. The performance of fuel cells with optimized pin-type designs was compared to traditional designs to assess the impact of these enhanced structures on overall fuel cell performance.

A review research [15] investigates performance studies of proton exchange membrane fuel cells (PEMFCs) with different flow field designs. The paper provides a detailed analysis of various conventional, modified, hybrid, and novel flow field configurations in PEMFCs. It also reviews the effects of factors such as channel tapering, channel bending, channel-to-landing width ratios, channel cross-sections, and the insertion of baffles, blockages, pin-fins, and inserts. While earlier studies primarily focused on conventional pin-type channel configurations with fixed dimensions in fuel cell cathodes, this research introduces a novel approach. A three-dimensional numerical model, incorporating the governing equations and electrochemical kinetics, has been developed to analyze how variations in channel and pin dimensions impact the performance of a fuel cell with a honeycomb pin-type flow field.

2 Mathematical Model

2.1 Description of the PEM fuel cell model with a honeycomb flow field

Figure 1 presents a depiction of a PEM fuel cell featuring an innovative honeycomb flow field. This configuration includes bipolar plates with pin-shaped channels, gas diffusion layers, catalyst layers, and a membrane. Hydrogen and air are supplied to the anode and cathode channels, respectively. The distinctive honeycomb design improves mass transport, thereby enhancing the cell's performance. The electric current generated, which is directly related to the cell's dimensions, is referred to as current density [16].

The flow channels are arranged in a honeycomb pattern using pin fins, where hexagonal pins are uniformly distributed across the flow field. These pins cause the gas flow within the channel to split into two orthogonal flow sets, in the x and y directions. A key advantage of the pin fin pattern is its low pressure drop. Additionally, in parallel and serpentine flow fields, liquid water formation within the fuel cell can lead to water accumulation or even channel blockage. The pin fin pattern is less prone to such issues, reducing the risk of channel blockage. The honeycomb pin fin pattern further minimizes water accumulation compared to the conventional pin fin design.

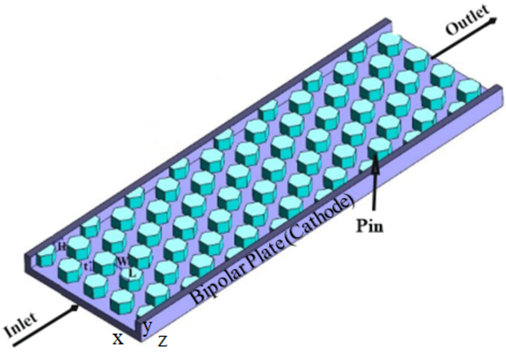

Fig. 1. 3D modeling domain of a single PEM fuel cell featuring a honeycomb flow field.

2.2 Governing equations

To streamline the resolution of the governing equations in the fuel cell model, several assumptions are made: (a) Gas mixtures are considered ideal, (b) The porous layers are treated as isotropic and homogeneous, (c) Given the low pressure and velocity gradients, the fluid flow is characterized as laminar and incompressible, (d) The losses due to contact resistance between various layers are disregarded, (e) A single-phase approach is utilized for water transport. The model integrates conservation equations pertaining for mass, momentum, species, charge, and energy, based on the assumptions outlined earlier. It simultaneously solves all governing equations across different regions of the fuel cell using a single-domain approach and a finite volume method. The advantage of using a single-domain model is that it eliminates the need to define boundary conditions at the interfaces between the cell's regions. Instead, boundary conditions are only required at the external boundaries of the model. This simplification improves the accuracy of the analysis and streamlines the solution process, although it may increase computational time. The governing equations, along with the corresponding source terms for various regions of the polymer electrolyte membrane fuel cell, are presented in Table 1.

Table 1. Equations governing fluid movement and electrochemical reactions across various areas of the PEM fuel cell, along with source and sink terms resulting from reaction rates and mass transfer [17].

Source or Sink Terms	The region with Source Term[1]	Mathematical form of the governing equation	Equation	
0	-	$\nabla \cdot (\rho \vec{u}) = 0$	Mass	(1)
$S_u = -\frac{\mu}{k}\vec{u}$	Gas diffusion layers and catalyst	$\frac{1}{\epsilon}\nabla \cdot (\rho \vec{u}\vec{u}) = -\nabla P + \nabla \cdot \tau + S_u$	Momentum	(2)
$S_k = -\frac{s_k j}{nF}$	Catalyst layers (reactors)	$\nabla(\vec{u}C_k) = \nabla \cdot (D_k^{\mathrm{eff}} \nabla C_k) + S_k$	Species	
$S_k = -\nabla \cdot \left(\frac{n_d}{F} I\right) - \frac{s_k j}{nF}$	Catalyst layers (water)			(3)
$S_\phi = j$	Catalyst layers	$\nabla \cdot (\kappa^{\mathrm{eff}} \nabla \phi_e) + S_\phi = 0$	Electrical potencies	(4)
$S_T = j\left(\eta + T\frac{dU_0}{dT}\right) + \frac{I^2}{\kappa^{\mathrm{eff}}}$	Catalyst layer	$\nabla \cdot (\rho C_p \vec{u} T) = \nabla \cdot (k^{\mathrm{eff}} \nabla T) + S_T$	Energy	
$S_T = \frac{I^2}{\kappa^{\mathrm{eff}}}$	Membrane			(5)
-	Catalyst layers	$\sum_k s_k M_k^z = ne^-$	Electrochemical reaction	(6)

Table 1 presents the governing equations for, in order; velocity vector ($\vec{u}$), fluid density (ρ), shear stress (τ), porosity (ϕ_e), pressure (P), concentration of species k (C_k), electric potential in the membrane (ϵ), effective thermal conductivity (k_{eff}), specific heat at constant pressure (C_p), effective diffusion coefficient of species k (D_k^{eff}), viscosity (μ), and temperature (T). In Equation (6), M_k represents the molecular weight of species k, s_k is the stoichiometric coefficient, and n is the number of electrons transferred, occurring at both the anode and cathode.

In regions with pores, the superficial velocity is used to ensure mass flux continuity at the boundary between porous and non-porous areas.

---

[1] In this column, for any region not explicitly mentioned, the source or sink term for that equation in that region is zero

The momentum equations include a source term that follows the Darcy equation, applicable under conditions of low permeability and velocity. The energy equation incorporates a source term to account for heat generation due to reactions, irreversibilities, and ohmic heating. In the species conservation equation, the source term reflects the generation or consumption of reactant species as well as water transport. The charge conservation equation contains a source term that represents the electric current flowing between the solid and electrolyte phases in both the anode and cathode catalyst layers. Table 2 provides the key properties and parameters necessary for solving the governing equations outlined in Table 1.

Table 2. Properties and terms required to solve the governing equations [18, 19].

Mathematical form of equation	Equation	
$j_a = \mathrm{aj}_{0,a}^{\mathrm{ref}}\left(\frac{C_{\mathrm{H}_2}}{C_{\mathrm{H}_2,\mathrm{ref}}}\right)^{\frac{1}{2}}\left(\frac{\alpha_a+\alpha_c}{RT}\times F\times\eta\right)$	Anode current density according to activation loss (Volmert-Butler equation)	(7)
$j_c = -\mathrm{aj}_{0,c}^{\mathrm{ref}}\left(\frac{C_{\mathrm{O}_2}}{C_{\mathrm{O}_2,\mathrm{ref}}}\right)^{\frac{1}{2}}\times\exp\left(\frac{-\alpha_c}{RT}\times F\times\eta\right)$	Cathode current density according to activation loss (Volmert-Butler equation)	(8)
$U_0 = \varphi_S - \varphi_e - U_0$	Overvoltage	(9)
$U_0 = 0$	Open circuit voltage on the anode side	(10)
$U_0 = 1.23 - 9.0\times 10^{-4}(T - 298.15)$	Open circuit voltage on the cathode side	(11)
$\mathrm{ai}_{0,c}^{\mathrm{ref}}(T) = \mathrm{ai}_{0,c}^{\mathrm{ref}}(353\,\mathrm{K})\times\exp\left[-16456\left(\frac{1}{T}-\frac{1}{353.15}\right)\right]$	Equilibrium potential	(12)
$D_k = D_0\left(\frac{T}{T_0}\right)^{\frac{3}{2}}\left(\frac{P_0}{P}\right)$	Diffusion coefficient of gases in non-porous areas as a function of temperature and pressure	(13)
$D_k^{\mathrm{eff}} = \varepsilon_i^{1.5}\times D_k$	Diffusion coefficient of gases in porous areas as a function of porosity coefficient	(14)
$D_{w,\mathrm{mem}} = \begin{cases} 3.1\times 10^{-7}\lambda(e^{0.28\lambda}-1)\,e^{(-2346/T)} & 0\le\lambda\le 3 \\ 4.17\times 10^{-8}\lambda(1+161e^{-\lambda})\,e^{(-2346/T)} & \lambda > 3 \end{cases}$	Water diffusion coefficient in the membrane	(15)
$K_{\mathrm{mem}} = (0.5139\lambda - 0.326)\exp\left[1268\left(\frac{1}{303}-\frac{1}{T}\right)\right]$	Membrane proton conductivity as a function of membrane relative humidity and temperature	(16)
$n_d = \frac{2.5\lambda}{22}$	Electro-osmotic drag coefficient of water as a function of membrane relative humidity	(17)
$\lambda = \begin{cases} 0.043 + 17.81a - 39.85a^2 + 36.0a^3 \\ 14 + 1.4(a-1) \end{cases}$	Membrane relative humidity as a function of water activity in the membrane	(18)
$a = \frac{C_W^g RT}{P^{\mathrm{sat}}}$	Water activity as a function of water concentration, temperature and water saturation pressure	(19)
$\rho C_P = \epsilon(\rho C_P)_f + (1-\epsilon)\cdot(\rho C_P)_S$	Effective heat capacity in porous materials including solid and liquid phase	(20)

To ensure continuous mass flux at the interface between porous and non-porous regions, an apparent velocity is introduced. The momentum equations include source terms that validate Darcy's law under conditions of low permeability and velocity. In the energy equation, the source terms account for heat generation resulting from reactions, irreversibilities, and ohmic heating. The source terms in the species conservation equation relate to the production or consumption of species, as well as the movement of water. Additionally, the source terms in the charge conservation equation represent the electric currents flowing between the solid and electrolyte phases within the anode and cathode catalyst layers.

2.3 Boundary conditions

Equations (1) to (5) presented in Table 1 constitute a comprehensive set of governing equations used to determine the unknown variables, including velocity components, pressure, concentrations of species (hydrogen, oxygen, nitrogen, and water), electrode potential, and temperature. Since a single-domain approach is employed, boundary conditions are required only at the external surfaces of the computational domain. In the z-direction, symmetry boundary conditions are applied to all surfaces adjacent to the channel. At the inlet, a specified mass flow rate boundary condition is set. The flow rate is determined based on the stoichiometric requirements for both the anode and cathode sides. The mass flow rates are computed and distributed according to the following relationships:

$$\dot{m}_{\text{in}} = \frac{\zeta_a I_{\text{ref}} A_{\text{MEA}}}{n_a F X_{\text{in}}^{\text{H}_2}} \tag{21}$$

$$\dot{m}_{\text{in}} = \frac{\zeta_c I_{\text{ref}} A_{\text{MEA}}}{n_c F X_{\text{in}}^{\text{O}_2}} \tag{22}$$

In the provided equations, A_{MEA} represents the geometric area of the membrane, A_{ch} indicates the cross-sectional area of the channel, and ζ denotes the stoichiometric coefficient of the current. The variable n signifies the number of electrons, F corresponds to Faraday's constant, and I_{ref} represents the reference current density. The concentrations of the inlet species (C_{kin}), along with the inlet pressure and humidity conditions, are specified at the inlets of both the anode and cathode. It is assumed that the temperature of the inlet gases aligns with the cell's operating temperature of 80 °C. At the outlets of the anode and cathode channels, a defined outlet pressure boundary condition is imposed. The flow conditions at the outlet boundaries are assumed to be fully developed or characterized by negligible flux. A no-slip condition is enforced on the velocity, while a zero-flux condition is applied to other variables at the walls. Additionally, a no-slip wall boundary condition is implemented on all surfaces of the pins connected to the current collector. For the electric potential equation, the potential is generally set to zero on the anode side, while the open-circuit voltage is applied at the cathode side.

2.4 Networking and numerical solution method

The computational mesh utilized for the complete modeling domain as well as for each individual pin, is shown in Figure 2. The mesh is refined in specific regions, including the gas diffusion layers, catalyst layers, and at the inlet and outlet of the channel. A structured mesh with hexahedral elements is applied to the model, while a mapped mesh is used for the pins, ensuring structured hexahedral elements throughout. An example of the meshing of a pin in the honeycomb configuration is also illustrated in Figure 2. A mesh independence study was conducted, focusing on the average current density at a voltage of 0.6 V. Four different meshes with 26,930, 144,473, 248,130, and 364,000 elements were analyzed. The results showed consistency at 248,130 computational cells, indicating that mesh size beyond this point did not significantly affect the outcomes. An iterative process using the SIMPLE algorithm was employed to solve the coupled pressure-velocity equations across the domain, with a second-order upwind scheme used for discretization. The governing equations were numerically solved using the commercial software ANSYS Fluent. To enhance convergence, an algebraic multigrid (AMG) technique is implemented. This method computes the solution over multiple grid levels to eliminate both high- and low-frequency errors. For the multigrid cycle, an F-cycle with a conjugate gradient stabilized smoother is used, with the maximum number of cycles limited to 60. By carefully selecting modeling parameters, the results show good agreement with experimental data from a real fuel cell. Table 3 provides the dimensions of the computational domain, along with the physical and chemical properties of the cell.

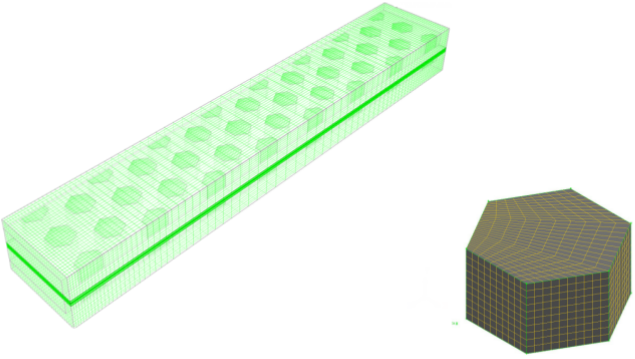

Fig. 2. Computational grid of the solution domain with structured discretization for the hexagonal pins.

Table 3. Geometric dimensions, operating conditions, transport coefficients, and material characteristics of the model [20–23].

Parameter	Unit	Value
Height, length and width of the channel	mm	60, 18 ,1.5
The thickness of the collector layer, gas diffusion layer, catalyst, and membrane	μm	1000, 260, 10, 230
The size of regular hexagonal pins	mm	1.5
Longitudinal distance between pins	mm	1.5, 1.3
Battery operating temperature	K	353.15
Anode and cathode pressure	Atm	1.5
Anode and cathode stoichiometry	-	1
Anode inlet channel mass flow	kg/s	7.33×10^{-6}, 1.413×10^{-4}
Mass fraction of hydrogen gas and input water in the anode channel	-	0.53, 0.47
Mass fraction of oxygen, nitrogen and input water in the cathode channel	-	0.11, 0.42, 0.47
Density of Anode and cathode exchanged current	A/m^2	2500, 0.006
Molar concentration of hydrogen and oxygen source	kmol/m^3	0.0564, 3.39×10^{-3}
Anode and cathode concentration power	-	0.5, 1
Anode and cathode charge transfer coefficient	-	2, 1
Anode gas viscosity, cathode gas viscosity	Pa s	1.101×10^{-5}, 1.881×10^{-5}
Viscosity of liquid water	Pa s	3.56×10^{-4}
The diffusion coefficient of hydrogen at 353K , 1.5 atm	m^2/s	9.15×10^{-5}
Oxygen diffusion coefficient at 353K , 1.5 atm	m^2/s	2.2×10^{-5}
water diffusion coefficient at 353K , 1.5 atm	m^2/s	2.56×10^{-5}
The diffusion coefficient of nitrogen at 353K , 1.5 atm	m^2/s	3×10^{-5}
Porosity of anode and cathode catalyst layer	-	0.28
Porosity of anode and cathode gas diffusion layer	-	0.3
Permeability of anode and cathode gas diffusion layer	m^2	1.76×10^{-11}
The contact angle of the anode and cathode gas diffusion layer	Degree	110
Surface to volume ratio	1/m	200000
Open circuit voltage	V	1.18
Thermal conductivity coefficient of hydrogen, oxygen, nitrogen and water vapor	W/m.K	0.2040, 0.0296, 0.0293, 0.0237
Thermal conductivity of collector/gas diffusion layer/catalyst layer	W/m.K	150
Thermal conductivity of the membrane	W/m.K	0.95
Electrical conductivity of collector/gas diffusion layer/catalyst	1/ohm.m	120

3 Results

3.1 Validation

The numerical simulation results of the simple channel fuel cell were validated against experimental data from Ticianelli [24] and are presented in Figure 3. A good agreement is observed between the numerical and experimental results, except at voltages below 0.4 V where the numerical model slightly overestimates the performance. This deviation is likely attributed to the onset of flooding, which is not captured in the single-phase model. Given that the pin-type flow field is less prone to flow separation, it is anticipated that this model will provide a more accurate representation of the experimental data, particularly at lower voltages.

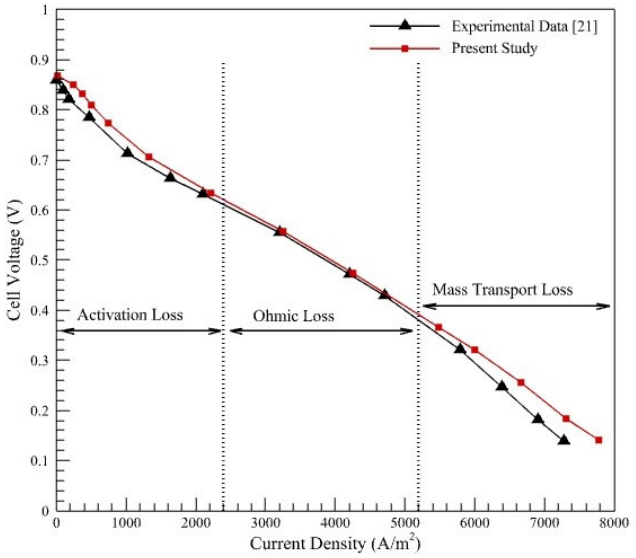

Fig. 3. Comparison of polarization curve simulation results and experimental results [24].

3.2 General results

Figure 4 presents the oxygen mole fraction distribution at the gas diffusion layer-catalyst layer interface. The distribution shows a non-uniform pattern, with higher oxygen concentrations near the inlet and lower concentrations near the outlet, which is due to oxygen consumption along the channel. The introduction of pins disrupts this pattern, leading to a more uniform oxygen distribution. This improved distribution enhances the electrochemical reaction kinetics by increasing the reactant surface area, which results in higher current densities and mitigates issues such as water flooding and the formation of local hot spots.

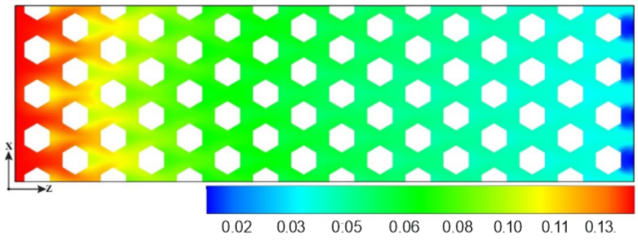

Fig. 4. Oxygen mole fraction distribution at the cathode GDL-CL interface, illustrating the impact of pin design on reactant distribution.

Water flooding significantly impacts the cost efficiency, durability, and performance enhancement of fuel cells. When the liquid water produced in the cathode – due to electro-osmotic drag and chemical reactions – exceeds the rate at which it can be removed through back-diffusion to the anode, evaporation, and transport from the gas diffusion layer, water flooding becomes more likely. This flooding hinders the movement of oxygen to the reaction sites, reducing the available active surface area of the catalyst and thereby impairing fuel cell performance. Consequently, water flooding accelerates the dissolution of platinum and carbon into the flow channel, exacerbating corrosion processes. To maintain optimal fuel cell functionality, it is crucial to remove the water that has migrated from the gas diffusion layer into the flow channel. Effective water management within the flow channels is therefore vital for ensuring the performance and longevity of fuel cells. A well-designed flow field is considered one of the most effective strategies for mitigating water flooding issues and promoting efficient water removal. Figure 5 illustrates the water mass fraction at the interface between the gas diffusion layer and the catalyst.

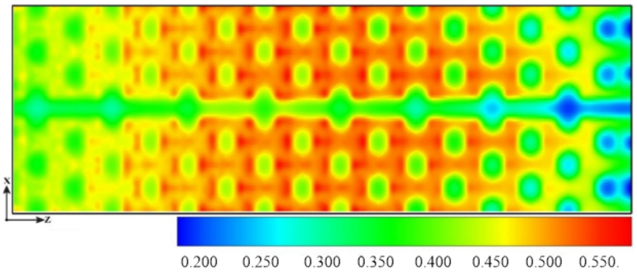

Fig. 5. Distribution of water mass fraction at the cathode side gas diffusion layer-catalyst interface.

The highest water mass fraction is observed in the central part of the channel, with significant water accumulation occurring in stagnant regions and vortices created by obstacles. Water content plays a crucial role in managing water flooding and localized hot spots within the fuel cell. When the water content exceeds 14% and approaches 22%, the likelihood of severe flooding in the gas diffusion layer and catalyst increases. As a result, many researchers are focusing on improving the uniformity of water distribution through optimized flow field designs to enhance overall fuel cell performance. The proton conductivity of the membrane is highly dependent on its water content, which directly influences fuel cell performance. Proper hydration of the membrane is essential for reducing resistance and minimizing ohmic losses within the cell. Humidifying the reactants effectively can enhance membrane hydration, while selecting the appropriate stoichiometry helps facilitate the removal of liquid water. Inadequate humidification, however, can disrupt temperature regulation within the cell. As membrane resistance increases, the output voltage decreases, requiring an increase in electrical current to maintain a consistent power output. This, in turn, leads to a rise in ohmic heat generation, further impacting the cell's efficiency. As a result, both cell temperature and the required cooling flow rates increase to manage the temperature, ultimately leading to a reduction in cell performance. External humidification is often employed when the water generated by the reactions is insufficient to fully hydrate the membrane, especially in the cathode inlet regions. However, excessive humidification can cause supersaturated vapor to condense into liquid water, which may clog the pores of the gas diffusion layer and obstruct the flow channels. This can increase the cell's electrical resistance and result in a decline in voltage. As shown in Figure 6, the water content predominantly remains below 14, which reduces the likelihood of water flooding in the gas diffusion layer.

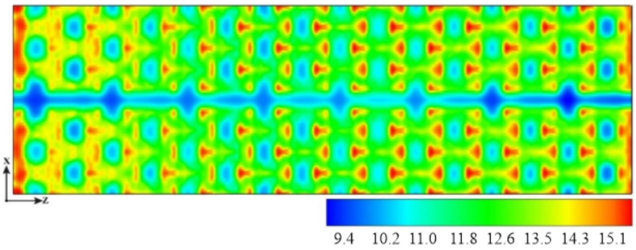

Fig. 6. Illustratation the distribution of water content at the boundary between the catalyst layer and the membrane on the cathode side.

Figure 7 presents the distribution of local current density within the channel at a cell voltage of 0.43 V. The elevated current density at the channel terminus is consistent with the co-current and counter-current flow regime, which contribute to enhanced oxygen utilization at the cathode inlet.

Variations in gas channel pressure have a significant influence on overall fuel cell performance. To suppress slug flow flow and promote droplet flow, higher inlet inertial forces are required. However, increasing the gas velocity also leads to a higher pressure drop within the channel, which in turn raises compressor power consumption. To improve cell performance, it is essential to remove the generated water, so increasing the gas inlet velocity is necessary to facilitate water transport. A trade-off between overall fuel cell performance and pressure drop is imperative. Figure 8 illustrates the pressure profile along the cathode channel. As oxygen is consumed in the cathode, the pressure decreases along the channel, but it increases due to wall shear stress and the presence of hexagonal obstacles. Pin-fin flow fields are characterized by a low pressure drop, as demonstrated in Figure 8, which shows a pressure drop of just 12.7 Pa across the channel. This drop is significantly lower than that observed in spiral channels [25, 26].

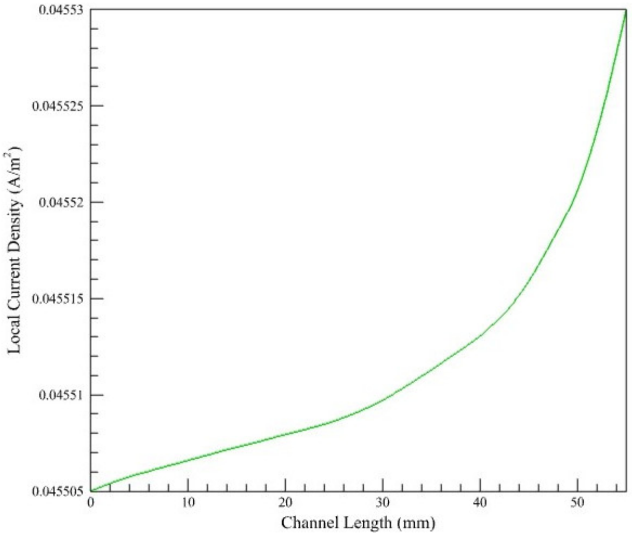

Fig. 7. Contribution of current density along the channel.

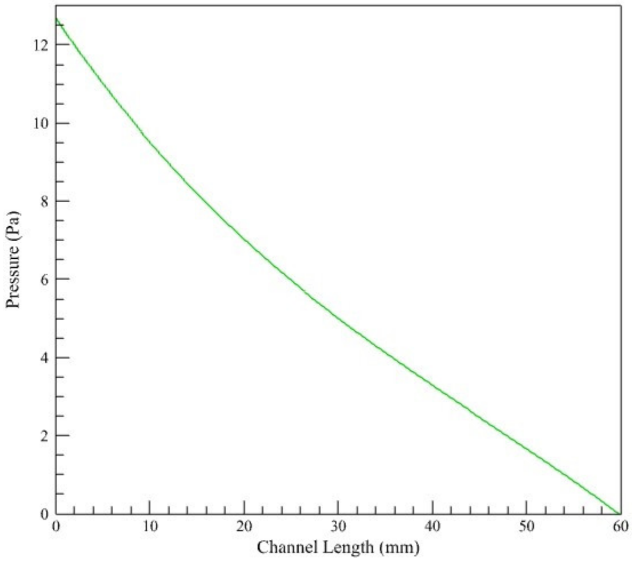

Fig. 8. Pressure contribution along the cathode channel.

3.3 Proposed translation options: The effect of the channel height-to-width ratio on the flow channel

The rectangular cross-section is the most commonly used shape for flow channels [27]. To examine the effect of the channel height-to-width ratio, three models with varying height-to-width ratios are analyzed, as shown in Table 4. In this table, "a" represents the channel height, and "b" represents the channel width.

Table 4. Dimensions of different channel cross-sections (dimensions in millimeters)

Parameters	Case 1	Case 2	Case 3
a (channel height)	1.0	1.0	0.8
b (channel width)	0.8	1.0	1.0

Figure 9a illustrates the significant impact of the channel height-to-width ratio on current density. When the ratio is increased from 0.8 to 1, current density rises by 7%, from 7000 A/m^2 to 7500 A/m^2. Further increasing the ratio from 0.8 to 1.25 results in a 14% boost in current density, reaching 8000 A/m^2. Analysis of polarization curves for different height-to-width ratios reveals that a ratio of 1.25, especially at higher current densities, leads to enhanced fuel cell performance. An increased channel height-to-width ratio enhances the mass transport of reactants to the catalyst layer, improving fuel cell performance. However, this higher ratio also increases the contact resistance between the bipolar plates and the membrane electrode assembly (MEA).

As a result, while the ratio significantly impacts the exchange current density, its effect on voltage drop is more limited, primarily due to constraints in mass transport. Figure 9b shows that the power density is lower for a channel height-to-width ratio of 0.8 and increases as the ratio grows. As mass transport limitations start to emerge, the maximum power density is observed at a current density of 3470 A/m^2. For a channel with a height-to-width ratio of 1.25, compared to one with a ratio of 1, the maximum power density shifts to a current density of 3890 A/m^2, representing a 4% increase, due to the onset of mass transport limitations at higher current densities.

By varying pin size and configuration within a honeycomb flow field, three models were studied to understand the resulting effects. In these models, the channel height and width were adjusted, while the pin dimensions and spacing were modified (Table 5).

Table 5. Summarizing the geometric parameters for each model.

Parameters (mm)	Title	Case 1	Case 2	Case 3
A	Gas channel width	6.0	12.0	9.0
B	The height of the gas channel	1.0	1.5	2.0
C	Current collector width	7.0	13.0	10.0
D	Height of current collector	1.0	1.0	1.0
E	The size of each regular pin	1.0	1.5	2.0
F	Longitudinal and transverse distance any regular pin	1.0	1.5	2.0

The effect of pin size on cell performance is clearly demonstrated in Figure 10. A pin size of 1.5 mm yields the best polarization and power density curves, suggesting enhanced gas diffusion. The maximum power density of 2500 W/m^2 at a current density of 5000 A/m^2 for the 1.5 mm pin size underscores its suitability for the base design.

The influence of pin diameter on pressure loss in the anode and cathode passages is shown in Figure 10a and Figure 10b.

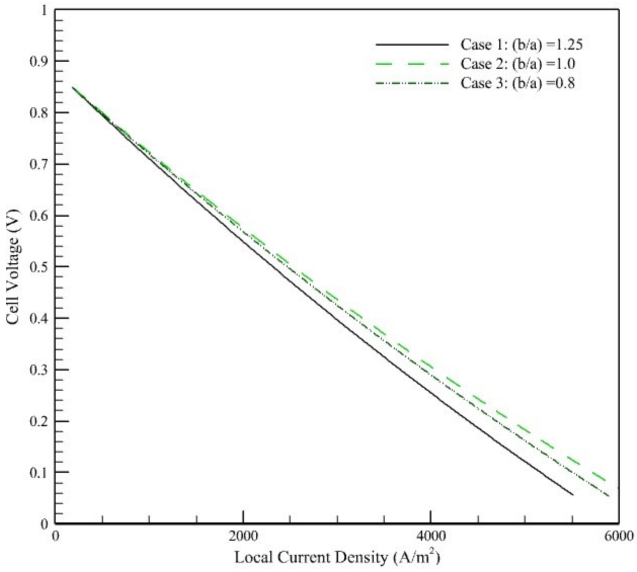

(a)

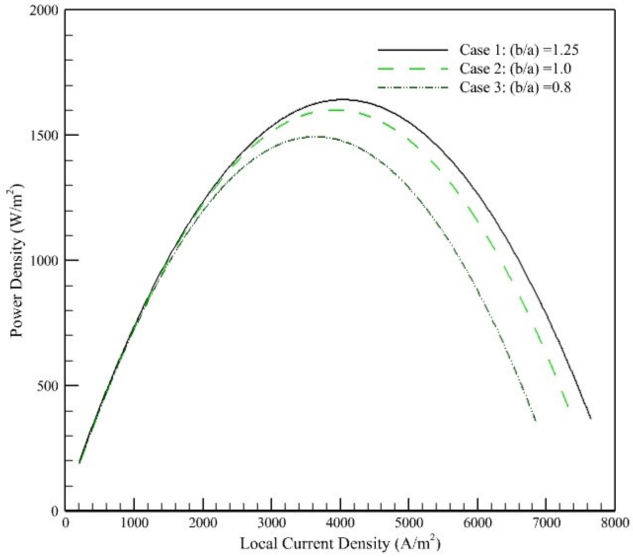

(b)

Fig. 9. Comparison of (a) polarization curves and (b) power density for different channel aspect ratios, highlighting the impact on cell performance.

The 1.5 mm pin results in the highest pressure loss in both the anode and cathode passages. While this increased pressure loss can aid in water removal from the anode, it may also elevate the power requirements of the blower. The higher pressure loss observed in the cathode is primarily due to the greater consumption of oxygen compared to hydrogen along the passage.

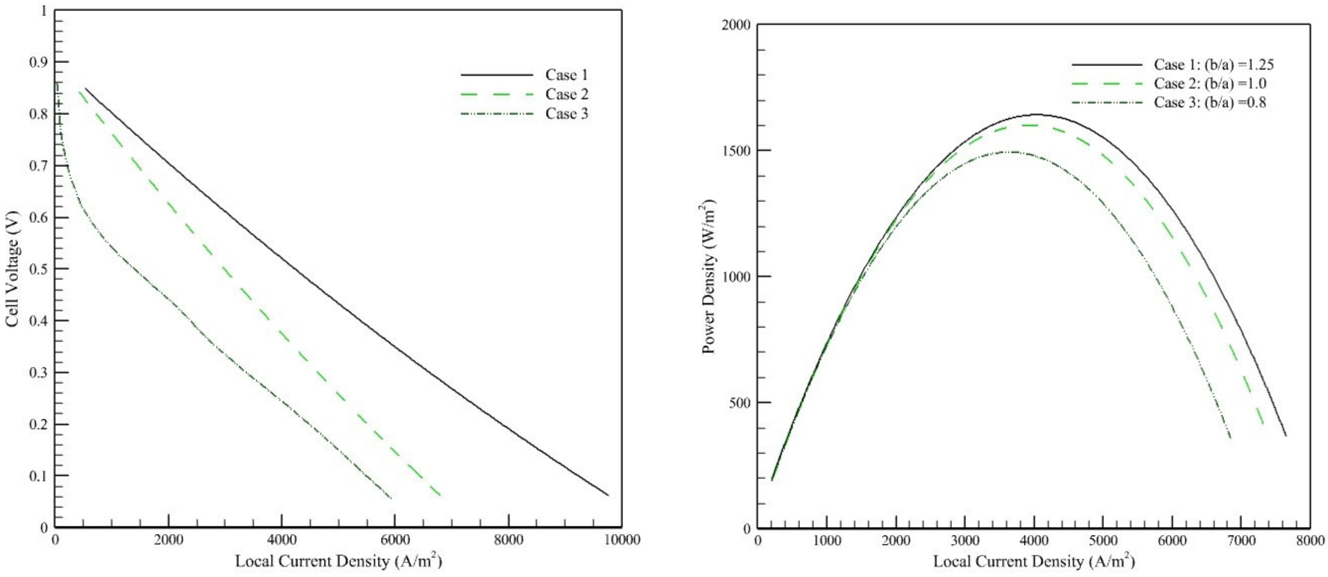

(a) (b)

Fig. 10. Performance comparison of different pin dimensions based on (a) polarization curves and (b) power density curves.

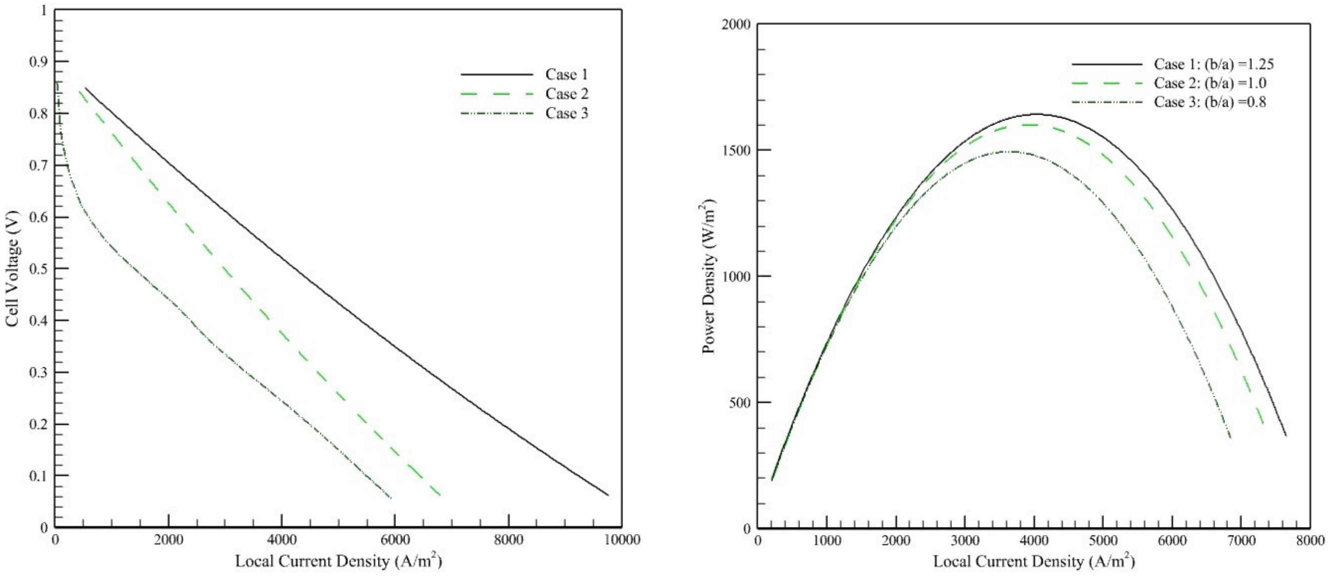

(a) (b)

Fig. 11. Overall pressure drop comparison along (a) the anode channel and (b) the cathode channel.

4 Conclusion

This research presents a comprehensive numerical analysis focused on optimizing the performance of a Polymer Electrolyte Membrane (PEM) fuel cell through the use of a honeycomb pin flow field. The study systematically explores the impact of various geometric and operational factors on cell performance. By strategically placing pins within the flow passages, the analysis demonstrates a significant improvement in oxygen distribution, leading to a more uniform reaction environment within the catalyst layer. This enhanced distribution helps to optimize electrochemical reactions, thereby improving overall fuel cell efficiency. This improved mass transport effectively mitigates common challenges in PEM fuel cell operation, such as localized water flooding and hot spots, which can significantly degrade performance. The numerical simulations further reveal that an optimal channel cross-sectional area ratio of 1.25, combined with a pin dimension of 1.5 mm, results in a marked reduction in pressure drop while maximizing power output. These findings offer crucial insights into the design and optimization of PEM fuel cells. The refined geometric parameters identified in this study serve as a valuable foundation for developing high-performance fuel cells with enhanced efficiency and longevity. Moreover, the numerical modeling approach employed in this research can be extended to investigate other flow field configurations and operational scenarios, offering a versatile framework for future advancements in fuel cell technology.

References

[1] Wang XD, Duan YY, Yan WM. Novel serpentine-baffle flow field design for proton exchange membrane fuel cells. Journal of Power Sources. 2007;173(1):210–221.

[2] Afshari E, Houreh NB. Numerical predictions of performance of the proton exchange membrane fuel cell with baffle (s)-blocked flow field designs. International Journal of Modern Physics B. 2014;28(16):1450097.

[3] Taymaz I, Benli M. Numerical study of assembly pressure effect on the performance of proton exchange membrane fuel cell. Energy. 2010;35(5):2134–2140.

[4] Atyabi SA, Afshari E. Three-dimensional multiphase model of proton exchange membrane fuel cell with honeycomb flow field at the cathode side. Journal of cleaner production. 2019;214:738–748.

[5] Reiser CA. Water and heat management in solid polymer fuel cell stack. Google Patents; 1989. US Patent 4,826,742.

[6] Hsieh SS, Yang SH, Kuo JK, Huang CF, Tsai HH. Study of operational parameters on the performance of micro PEMFCs with different flow fields. Energy Conversion and Management. 2006;47(13-14):1868–1878.

[7] Maia LK, Sousa Jr Rd. Three-dimensional CFD modeling of direct ethanol fuel cells: evaluation of anodic flow field structures. Journal of Applied Electrochemistry. 2017;47:25–37.

[8] Wang Z, Tongsh C, Wang B, Liu Z, Du Q, Jiao K. Operation characteristics of open-cathode proton exchange membrane fuel cell with different cathode flow fields. Sustainable Energy Technologies and Assessments. 2022;49:101681.

[9] Lobato J, Canizares P, Rodrigo MA, Pinar FJ, Úbeda D. Study of flow channel geometry using current distribution measurement in a high temperature polymer electrolyte membrane fuel cell. Journal of Power Sources. 2011;196(9):4209–4217.

[10] Vaz WS. Multiobjective Optimization of Pin-Type Flow Channels Using a Reinterpretation of Murray's Law. Electronics. 2021;10(14):1698.

[11] Toghyani S, Atyabi SA, Gao X. Enhancing the specific power of a pem fuel cell powered uav with a novel bean-shaped flow field. Energies. 2021;14(9):2494.

[12] Yan WM, Mei SC, Soong CY, Liu ZS, Song D. Experimental study on the performance of PEM fuel cells with interdigitated flow channels. Journal of Power Sources. 2006;160(1):116–122.

[13] Thitakamol V, Therdthianwong A, Therdthianwong S. Mid-baffle interdigitated flow fields for proton exchange membrane fuel cells. International journal of hydrogen energy. 2011;36(5):3614–3622.

[14] Guo N, Leu MC, Koylu UO. Network based optimization model for pin-type flow field of polymer electrolyte membrane fuel cell. International journal of hydrogen energy. 2013;38(16):6750–6761.

[15] Marappan M, Palaniswamy K, Velumani T, Chul KB, Velayutham R, Shivakumar P, et al. Performance studies of proton exchange membrane fuel cells with different flow field designs–review. The Chemical Record. 2021;21(4):663–714.

[16] Baharlou-Houreh N, Masaeli N, Afshari E, Mohammadzadeh K. Performance analysis of a proton exchange membrane fuel cell with the stair arrangement of obstacles in the cathode channel. International Journal of Numerical Methods for Heat & Fluid Flow. 2023;33(12):3940–3966.

[17] Afshari E. Computational analysis of heat transfer in a PEM fuel cell with metal foam as a flow field. Journal of Thermal Analysis and Calorimetry. 2020;139(4):2423–2434.

[18] Wang Y, Wang CY. Transient analysis of polymer electrolyte fuel cells. Electrochimica Acta. 2005;50(6):1307–1315.

[19] Masaeli N, Afshari E, Baniasadi E, Baharlou-Houreh N. Performance studies of a membrane-based water and heat exchanger using serpentine flow channels for polymer electrolyte membrane fuel cell application. Applied Thermal Engineering. 2023;222:119950.

[20] Ju H, Meng H, Wang CY. A single-phase, non-isothermal model for PEM fuel cells. International Journal of Heat and Mass Transfer. 2005;48(7):1303–1315.

[21] Pei P, Chen H. Main factors affecting the lifetime of Proton Exchange Membrane fuel cells in vehicle applications: A review. Applied Energy. 2014;125:60–75.

[22] Carton J, Lawlor V, Olabi A, Hochenauer C, Zauner G. Water droplet accumulation and motion in PEM (Proton Exchange Membrane) fuel cell mini-channels. Energy. 2012;39(1):63–73.

[23] Sierra J, Figueroa-Ramírez S, Díaz S, Vargas J, Sebastian P. Numerical evaluation of a PEM fuel cell with conventional flow fields adapted to tubular plates. International journal of hydrogen energy. 2014;39(29):16694–16705.

[24] Ticianelli EA, Derouin CR, Srinivasan S. Localization of platinum in low catalyst loading electrodes to to attain high power densities in SPE fuel cells. Journal of electroanalytical chemistry and interfacial electrochemistry. 1988;251(2):275–295.

[25] Pasaogullari U. Heat and water transport models for polymer electrolyte fuel cells. Handbook of fuel cells. 2010;.

[26] Hashemi F, Rowshanzamir S, Rezakazemi M. CFD simulation of PEM fuel cell performance: ef-

fect of straight and serpentine flow fields. Mathematical and Computer Modelling. 2012;55(3-4):1540–1557.

[27] Manso A, Marzo F, Barranco J, Garikano X, Mujika MG. Influence of geometric parameters of the flow fields on the performance of a PEM fuel cell. A review. International journal of hydrogen energy. 2012;37(20):15256–15287.